ISSN (Print) 1226-1750
ISSN (Online) 2233-6656
Journal of Magnetics 27(4), 366-372 (2022) https://doi.org/10.4283/JMAG.2022.27.4.366

Influence of the Electrolytic Dy-Cu alloy on the Coercivity of Sintered Nd-Fe-B Magnet

Chun-fa Liao[1,2]*, Xun Zhou[1,2]*, Peng Jiang[1,2], Zhiyong Zeng[1,2], and Lianghua Que[1,2]

[1]*Faculty of Materials Metallurgy and Chemistry, Jiangxi University of Science and Technology, Ganzhou 341000, China*
[2]*National Innovation Center for Rare Earth Functional Material, Jiangxi University of Science and Technology, Ganzhou 341000, China*

(Received 2 August 2022, Received in final form 17 October 2022, Accepted 2 November 2022)

The fluorine salt oxide molten-salt electrolytic Dy-Cu alloy was used as a grain boundary diffusion source instead of the doped Dy-Cu alloy. The microstructure and coercivity of the GBDPed magnets with the different diffusion times were studied. The results show that the coercivity increased with the increase in the GBDP time. The ability of the electrolytic Dy-Cu alloy to improve the coercivity of Nd-Fe-B is more advantageous than that of the doped Dy-Cu alloy. Microstructure analysis shows that the segregation and metal inclusion, a small amount of Dy_2O_3, and the poor synergy diffusion between Dy and Cu lead to the unsatisfactory performance of the doped Dy-Cu alloy to improve the coercivity. The diffusion rate and depth of the GBD source improved by replacing the doped alloy with an electrolytic alloy.

Keywords : sintered Nd-Fe-B magnets, molten salt electrolysis, grain boundary diffusion, heat treatment time, coercivity

1. Introduction

Among the existing magnetic materials, sintered NdFeB magnets show the highest magnetic energy product, which arises from the excellent intrinsic magnetic properties of Nd2Fe14B unit cells [1-4]. To ensure sintered NdFeB has enough coercivity at the target working temperature. In the production of sintered NdFeB, the preferred additives are Dy [5-8] and Dy-based [9-15] alloys. The industrial application of the grain boundary diffusion process (GBDP) not only significantly improves the coercive force of the magnet but also sharply reduces the amount of Heavy Rare Earth, which is cost-effective for the process. However, the diffusion depth of Heavy Rare Earth along the thickness direction of the magnet is limited, and how to improve its diffusion rate is a critical problem [15].

Compared with the doped alloys, the low melting point Dy alloys prepared by molten salt electrolysis are mainly single-phase master alloys [16]. It can more effectively reduce the self-diffusion activation energy of the diffusing agent, provide a smoother diffusion channel, increase the diffusion rate [15] and supply a more cost-effective diffusion process for the actual demand. With the help of molten salt electrolysis, the process of "REO/Cl/F - RE metal - RE alloy - Diffusion treatment" would simply to "REO/Cl/F - RE alloy - Diffusion treatment."

Based on the above considerations, the Dy-Cu alloy prepared by molten salt electrolysis replaces the doped Dy-Cu alloy for grain boundary diffusion research in this paper. The morphology and chemical composition along the magnet thickness direction and the diffusion behavior of Dy and Cu in the magnet were characterized to clarify the influence of the electrolytic Dy-Cu alloy in the sintered Nd-Fe-B magnet.

2. Materials and Methods

Commercial sintered Nd-Fe-B magnets purchased from Ganzhou FORTUNE Electronics Co., Ltd. machined into a 10 mm × 10 mm × 5 mm cube. The electrolytic Dy-Cu alloy made from LiF-DyF_3-Dy_2O_3(2 wt.%)-Cu_2O(1 wt%) molten-salt system. Electrolysis was carried out at 950 °C for 4 hours with a constant current of 20 A. In this work, the graphite crucible was used as the anode, and a

**Co-corresponding author: Tel: +86-0797-8312332
Fax: +86-0797-8312332, e-mail: liaochfa@163.com
Tel: +86-13576812819, Fax: +86-13576812819
e-mail: 13576812819@163.com

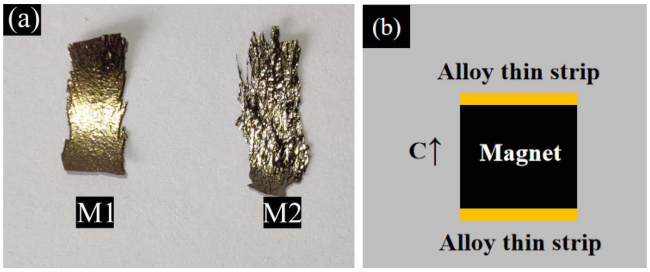

Fig. 1. (Color online) (a) Alloy thin strip; (b) A diffusion couple formed by covering a magnet with an alloy thin strip.

tungsten rod as the cathode. The tungsten crucible was selected as the receiving crucible, and placed in the boron nitride crucible to prevent the tungsten crucible from contacting the graphite crucible. In this study, pure metal Dy and Cu were used as raw materials, vacuumed to below 5.0×10^{-3} Pa, melting in an argon atmosphere to produce the doped Dy-Cu alloy. Subsequently, the Dy-Cu alloy thin strips made by the melt rapid quenching technique respectively marked as M1 and M2. As shown in Fig. 1(a), the Dy-Cu alloy M1 was made by molten-salt electrolysis. The magnet and alloy strips were polished with sandpaper, cleaned with ethanol, and dried in a vacuum oven before use. The upper and lower surfaces of the magnet were covered with an alloy strip to form a diffusion couple. The diffusion source penetrated in a direction parallel to the C-axis, as shown in Fig. 1(b).

The alloy samples were analyzed by X-ray diffractometer (XRD). The melting points of the alloy samples were determined from differential thermal gravimetry (DTG). The magnetic properties were measured using a high-temperature permanent magnet measuring instrument (NIM-500C type). The surface and cross of the magnet were imaged after the GBDP using a scanning electron microscope (SEM) with energy dispersive spectroscopy (EDS) to characterize the morphology and chemical distribution.

3. Results and Discussion

3.1. Grain boundary diffusion source

M1 and M2 are composed of an intermetallic compound DyCu and solid solution β-Dy at room temperature. Compared with M1, M2 has solid solution β-Dy as the majority diffraction peaks, and several diffraction peaks of Dy_2O_3 are observed, as shown in Fig. 2. Owing to the segregation phenomenon of M2, a few Dy which did not alloy with Cu were oxidized to Dy_2O_3. The analysis of X-ray diffraction patterns shows that M1 has a uniform alloying, and there may be synergistic diffusion between

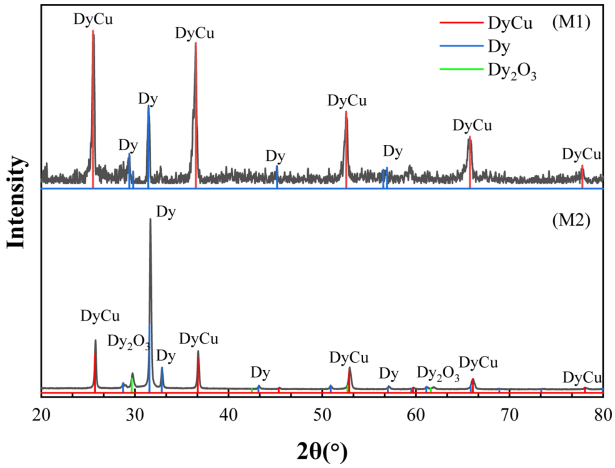

Fig. 2. (Color online) XRD pattern of Dy-Cu binary alloy diffusion source.

Dy and Cu, which is conducive to reducing the activation energy of self-diffusion.

ICP-MS analysis shows that the composition of M1 is $Dy_{67}Cu_{33}$ (at.%), and that of M2 is $Dy_{70}Cu_{30}$ (at.%). As shown in Fig. 3, the melting point of M1 is 796.5 °C higher than 791.1 °C because $Dy_{70}Cu_{30}$ (at.%) is a binary eutectic point. Therefore, M1 and M2 can melt at the diffusion temperature of 950 °C. Low melting point eutectic alloys are the most common choice. Thus, we chose $Dy_{70}Cu_{30}$ as the component for the doped alloy. It's easier to control the alloy composition when preparing Dy-based alloys from pure metal elements. In contrast, preparing Dy-Cu alloys with a content of 70:30 by molten-salt electrolysis is hard to control. For practical application, we prepared $Dy_{67}Cu_{33}$ by molten-salt electrolysis with the composition closest to $Dy_{70}Cu_{30}$.

3.2. Magnetic properties

Fig. 4 shows the variation curve of magnetic properties of the magnet diffused at different times (1, 2, 4, 6 hours) at 950 °C and annealing 3 hours at 550 °C. Within 4-6 hours of GBDP time, the coercivity of the GBDPed magnets with M1 increased significantly, while the coercivity of the GBDPed magnets with M2 did not change. Combined with XRD analysis, it is deduced that the undiffused β-Dy phase accounts for the majority during the M2 diffusion process. Before the β-Dy phase replaced Nd atoms and diffused into the magnet, there was a process of forming low melting point compounds with Nd and Cu in the grain boundary phase. In contrast, the β-Dy of M1 had little effect on the diffusion process.

The demagnetization curves and magnetic performance parameters of the corresponding magnets show in Fig. 5 and Table 1. The coercivity of the GBDPed magnets with

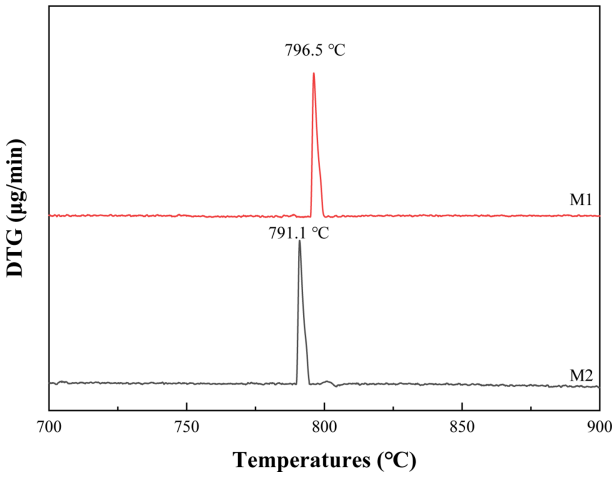

Fig. 3. (Color online) DTG curve of Dy-Cu alloys strip heated to 1000 °C at room temperature by 10 °C/min.

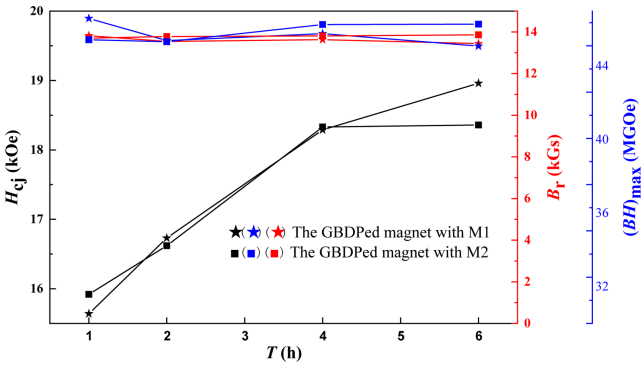

Fig. 4. (Color online) Variation curve of magnetic properties of Dy-Cu alloy diffusion treated magnets with the heat treatment time.

M1 and M2 increased to 19.0 kOe and 18.3 kOe, respectively. M2 contains a few O, which would deteriorate the coercivity [17]. Therefore, compared with the GBDPed magnet with M2, the GBDPed magnets with M1 performed with high coercivity.

The variation of remanence shows the differences between the GBDPed magnet with M1 and the GBDPed magnet with M2. Table 1 shows the remanence of the GBDPed magnet with M1 decreased significantly with the increase in GBDP time, reduced from 14.2 kGs to 13.4 kGs. Based on the above speculation, the content of Dy in the surface grains of the magnet is higher, leading to the remanence decrease. The remanence of the GBDPed magnet with M2 was significantly reduced, compared with that of the original magnet, but it hardly changed with increasing diffusion time. As reported, the amount of Dy in M2 infiltrated into the magnet is limited [18], which makes the remanence almost unchanged. The surface of the magnet was slightly polished to remove the deteriorated surface layer [19], which also affected the remanence.

After the GBDP with M1, the squareness degraded to poor 84.9 %. A non-uniform distribution of the HRE is a characteristic of the patch GBDP [15]. Highlight that the squareness of the GBDPed magnet with M2 is worse, only 77.9 %. With the extension of the GBDP time, changes in the microstructure of magnets and the diffusion path of Dy occurred in the diffusion region [20]. With the increase in GBDP times, the squareness difference between the M1 diffusion magnet and the M2 diffusion magnet is more significant. The distributions of Dy and Cu along diffusion depth are analyzed below to clarify the difference in magnetic properties.

3.3. Microstructure

There are three main diffusion behaviors of Dy in the GBDP. Firstly, Dy diffuses from the diffusion source body to the intergranular phase, then from the grain boundary phase to the matrix phase epitaxial layer to form the Dy-rich shell phase [5, 21]. With the extension of heat treatment time, Dy will diffuse from the Dy-rich shell phase to the Nd-Fe-B matrix phase [10, 22]. To explore the diffusion behavior of M1 and M2 at the initial stage of the GBDP and to clarify the reason for the different diffusion rates caused by this difference, the diffusion surface of the GBDPed magnets at 950 °C - 1 h + 550 °C - 3 h as for morphology characterization and

Table 1. The room temperature coercivity H_{cj}, remanence B_r, variation of coercivity and remanence of the GBDPed magnet with M1 (M2) at 950 °C for 1 - 6 h + 550 °C for 3 h.

Sample	Original	1 h	2 h	4 h	6 h
H_{cj} (kOe)	12.1	15.6 (15.9)	16.7 (16.6)	18.3 (18.3)	19.0 (18.3)
B_r (kGs)	14.2	13.8 (13.7)	13.5 (13.8)	13.6 (13.9)	13.4 (13.9)
$\Delta H_{cj}/H_{cj}$ (%)	-	28.9 (31.4)	38.0 (37.2)	51.2 (51.2)	57.0 (51.2)
$\Delta B_r/B_r$ (%)	-	-2.8 (-3.5)	-4.9 (-2.8)	-4.2 (-2.1)	-5.6 (-2.1)
Squareness (%)	97.6	86.1 (84.0)	85.3 (82.2)	86.7 (81.7)	84.9 (77.9)

(*) The data in brackets represent H_{cj} and $\Delta H_{cj}/H_{cj}$ of the GBDPed magnets with M2

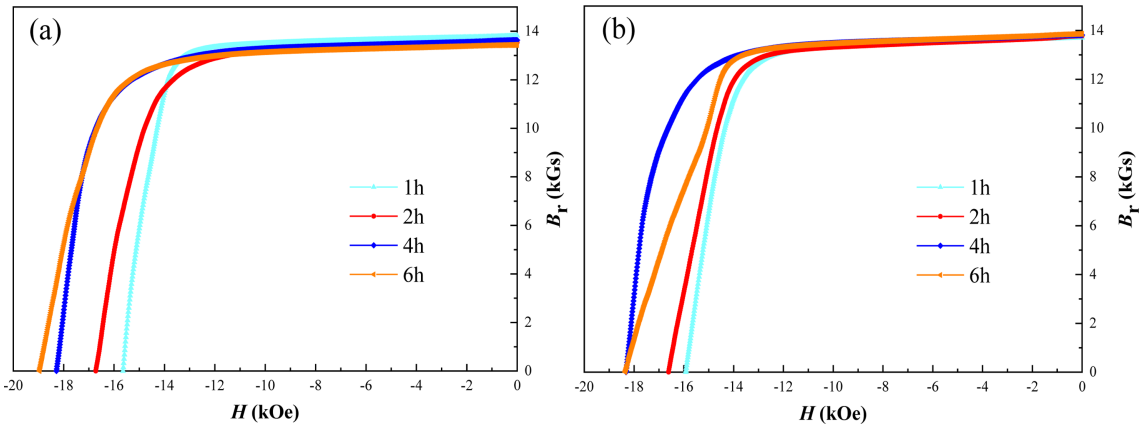

Fig. 5. (Color online) Demagnetization curve of the GBDPed magnet (a) GBDP with M1; (b) GBDP with M2.

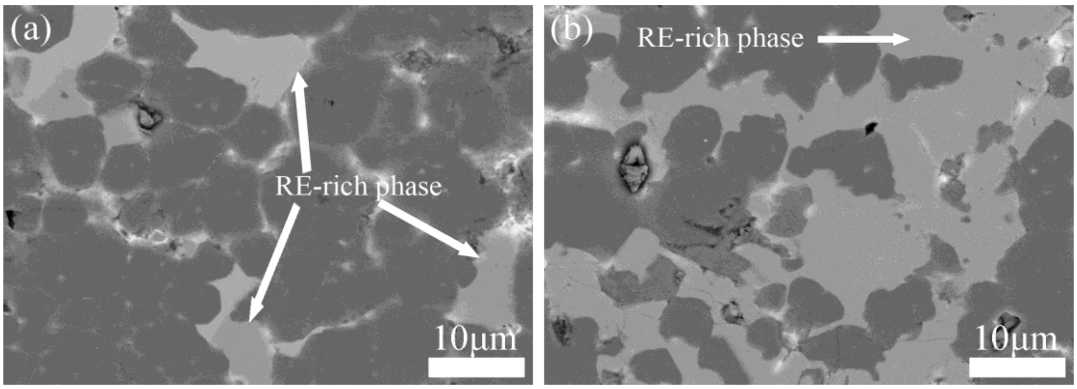

Fig. 6. SEM image of the diffusion surface of the GBDPed magnet at 950 °C - 1 h + 550 °C - 3 h, with the diffusion direction perpendicular to the paper face inward (a) GBDP with M1; (b) GBDP with M2.

composition analysis.

It can be seen from Fig. 6(a) that there are three areas: the large bright areas, the dark matrix areas, and the bright areas between dark particles at 950 °C - 1 h + 550 °C - 3 h. The volume fraction of RE-rich phases occupies more in the GBDP magnets with M2. The remanence comparison results correspond with Table 1. The remanence of the magnet treated with M1 is lower than that with M2. To compare the differences between M1 and M2 in different diffusion stages of Dy, using the GBDPed magnet at 950 °C - 6 h + 550 °C - 3 h as samples. The microstructures at 100 μm, 200 μm, and 400 μm away from the diffusion surface were characterized as shown in Fig. 7.

In Fig. 7(a), the Nd-rich phase further aggregated in the triple junction region, even inside the matrix phase. The aggregated Nd comes from the layered grain boundary phase between NdFeB grains [17, 23], and the Nd originates from the substitution of Dy [24-26]. In Fig. 7(b), the core-shell structure is visible, and the bright color region mainly exists in the intergranular phase. Fig. 7(a) and Fig. 7(b) show that the diffusion of Dy was in different stages at 100 μm from the diffusion surface. The core-shell structure is observed in both Fig. 7(c) and Fig. 7(d), but it is worth noting that the Nd-rich phase in Fig. 7(c) more evenly distributes around the matrix grains and the boundary between the matrix phase is clearer. It indicates that M1 diffused more fully at 200 μm from the diffusion surface. Only slight shell phases exist in the grains on the left side of Fig. 7(e), while no core-shell structure is observed in Fig. 7(f). For the GBDPed magnet with M2, the microstructure at 400 μm is similar to the original magnet.

The microstructure analysis of the magnet shows that the diffusion degrees of M1 and M2 are different along the diffusion depths. The GBDPed magnet with M1 achieved a higher diffusion uniformity at 950 °C - 6 h + 550 °C - 3 h, consistent with its coercivity enhancement and squareness in Table 1, but difficult to intuitively determine which is better. Therefore, in the circular regions selected in Fig. 7, we chose three points from the grain boundary phase, the shell phase, and the matrix

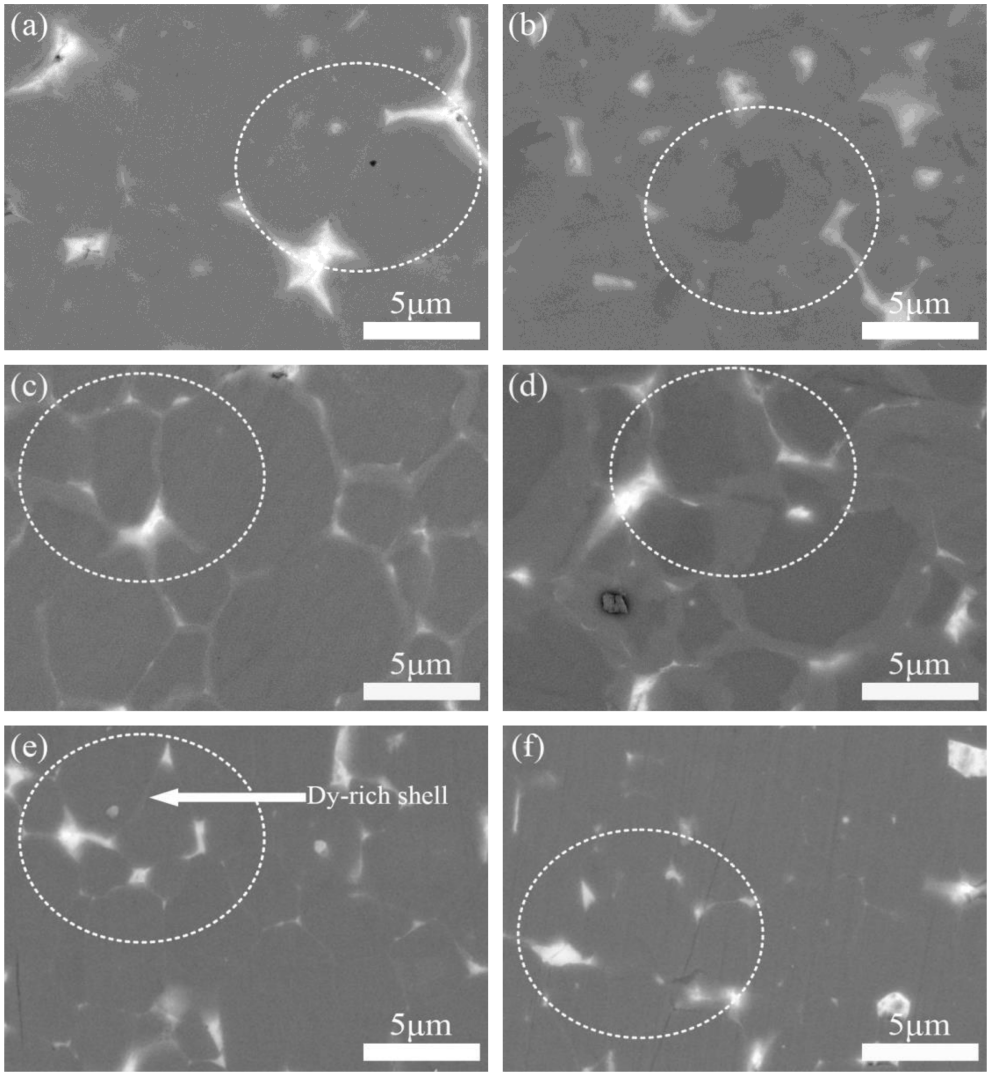

Fig. 7. SEM diagram of the GBDPed magnet along the thickness direction of the magnet (a), (b): 100 μm; (c), (d): 200 μm: (e), (f): 400 μm; the diffusion direction is from left to right, GBDP with M1 in the left column and GBDP with M2 in the right column.

phase, respectively. The average value of each sample was calculated, as shown in Fig. 8 and Fig. 9, and the changes in Dy and Cu content at 100 μm, 200 μm, and 400 μm from the diffusion surface were studied (the original magnet doesn't contain Dy and Cu).

As shown in Fig. 8(a), for the GBDPed magnet with M1, the diffusion of Dy from the shell to the main phase grain was dominant at 100 μm; at 200 μm, the content of Dy in the Dy-rich shell is the highest, and the formation of Dy-rich shell phase was dominant. Meanwhile, the content of Dy in the matrix phase is 0.10, meaning Dy had begun to diffuse into the matrix phase; at 400 μm, the formation of the Dy-rich shell phase dominated in the GBDP. As Fig. 8(b) shows, for the GBDPed magnet with M2, under different diffusion depths, Dy content decreases with the increase of diffusion depth, and 400 μm is the diffusion limit of Dy. From the analysis of Fig. 6 and Fig. 7, Dy concentrated in the Nd-rich intergranular corner phase, and the Nd-O compound would hinder the diffusion of Dy [6, 27]. XRD shows the presence of oxygen in M2, which is bound to deepen this effect. The result indicates that the diffusion rate and depth increased by replacing the doped alloy with the electrolytic alloy. Corresponding to Fig. 4, the improvement of coercivity by M1 is significantly better than that by M2.

RE-Cu alloys permeate into the grain boundary, forming low melting point intergranular phases such as Nd-Cu [28], Pr-Cu [29], (Nd, Dy)-Cu [11], and so on. The distribution of Cu in intergranular phases with different diffusion depths was studied. As shown in Fig. 9, the content of Cu in the intergranular phase decreased with increasing diffusion depth. It is worth noting that with the

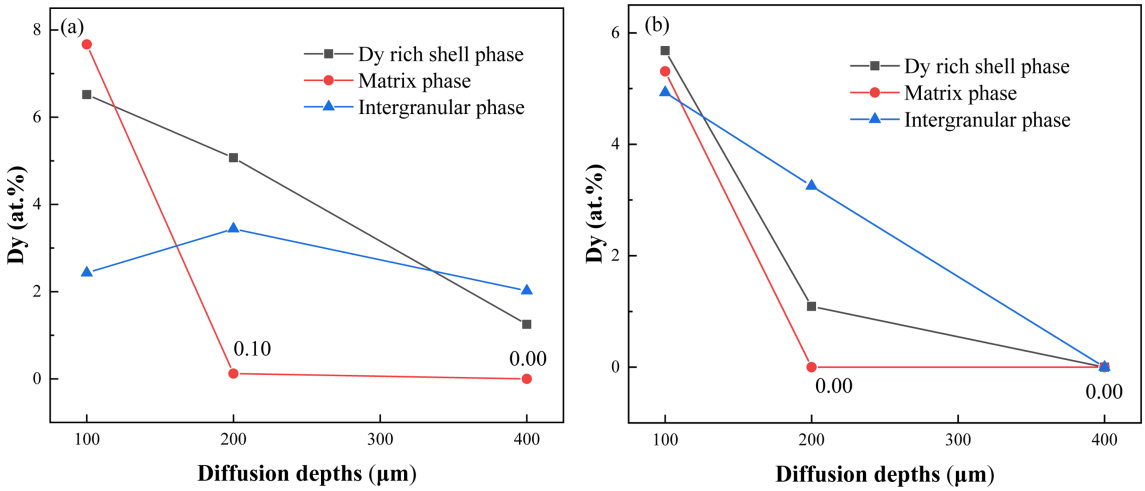

Fig. 8. (Color online) Distribution of Dy at different diffusion depths of magnets (a) GBDP with M1; (b) GBDP with M2.

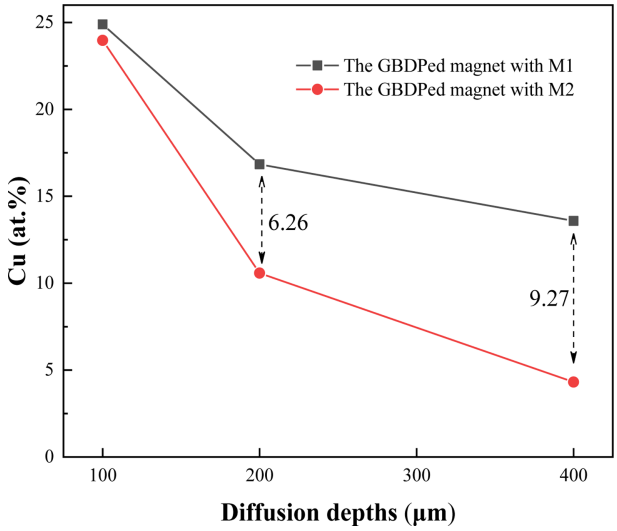

Fig. 9. (Color online) Distribution of Cu at different diffusion depths of the GBDPed magnet.

increase of diffusion depth, the difference in Cu content increased, indicating that the diffusion ability of Cu in M1 is superior. Dy and Cu in the electrolytic alloy are more effectively alloyed to form a single intermediate alloy phase, and the synergistic effect is intenser. Cu is easy to diffuse, which drives the diffusion of Dy. At 400 μm, about 15 % Cu was detected in the intergranular phase. It formed the low-melting-point grain boundary phase with Nd and provided the channel for Dy to diffuse to the deep of the magnet. Therefore, increasing the diffusion time is expected to further improve the diffusion depth of Dy along the thickness direction of the magnet, to prepare high-coercivity permanent magnets.

At the same GBDP time, the diffusion rate and depth of the electrolytic Dy-Cu alloy are better than those of the doped Dy-Cu alloy. In subsequent work, two-step eutectic GBDP with low eutectic alloys made by molten-salt electrolysis will be used to achieve higher remanence and squareness.

4. Conclusions

The results show that it is a feasible way to prepare high-performance sintered Nd-Fe-B by the GBDP with the electrolytic Dy-Cu alloy instead of the doped Dy-Cu alloy, and the following conclusions were obtained:

When the GBDP time is in the range of 4 to 6 h, the improvement of the coercivity of the magnet by the electrolytic alloy is more advantageous. Therefore, replacing the doped Dy-Cu alloy with an electrolytic Dy-Cu alloy can further improve the coercivity of the sintered Nd-Fe-B magnet.

The diffusion degree of the electrolytic alloy at different depths is better than that of the doped alloy, and the Dy in the electrolytic alloy diffuses deeper. Therefore, the electrolytic Dy-Cu alloy can increase the diffusion rate of the diffusion source to improve the diffusion depth.

Dy and Cu in the electrolytic alloy are more effectively alloyed to form a single intermediate alloy phase, and the synergistic effect is intenser. Cu is easy to diffuse, which drives the diffusion of Dy.

Acknowledgement

This work was funded by the National Natural Science Foundation of China (No. 51674126) and the Key R&D Foundation of Ganzhou-Documents of Ganzhou Science and Technology Bureau[2019]60.

References

[1] M. Sagawa, S. Fujimura, N. Togawa, and Y. Matsuura, J. Appl. Phys. **55**, 2083 (1984).

[2] S. Sugimoto, J. Phys. D: Appl. Phys. **44**, 064001 (2011).

[3] S. Z. Zhou, Q. F. Dong, and X. X. Gao, Sintered Nd-Fe-B rare earth permanent magnet materials and technology, Metallurgical Industry Press, Beijing (2021) pp 82.

[4] M. G. Zhu and W. Li, Rare Earth Information. **10**, 10 (2016).

[5] T. H. Kim, T. T. Sasaki, T. Ohkubo, Y. Takada, A. Kato, Y. Kaneko, and K. Hono, Acta Mater. **172**, 139 (2019).

[6] L. J. Zhang, S. D. Mao, L. J. Yang, Y. L. He, Z. L. Song, and C. Xu, Chinese Rare Earths. **39**, 90 (2018).

[7] X. Cheng, J. Li, L. Zhou, T. Liu, X. Yu, and B. Li, J. Rare Earths. **37**, 398 (2019).

[8] L. H. Liu, H. Sepehri-Amin, T. Ohkubo, M. Yano, A. Kato, N. Sakuma, T. Shoji, and K. Hono, Scr. Meter. **129**, 44 (2017).

[9] M. Tang, X. Bao, K. Lu, L. Sun, J. Li, and X. Gao, Scr. Mater. **117**, 60 (2016).

[10] H. Y. Liu, G. Wang, Y. Hong, and D. C. Zeng, Acta Metall. Sin. (Engl. Lett.). **31**, 496 (2017).

[11] H. Sepehri-Amin, J. Liu, T. Ohkubo, K. Hioki, A. Hattori, and K. Hono, Scr. Mater. **69**, 647 (2013).

[12] J. Fliegans, C. Rado, R. Soulas, L. Guetaz, O. Tosoni, N. M. Dempsey, and G. Delette, J. Magn. Magn. Mater. **520**, 167280 (2021).

[13] X. L. Liu, X. J. Wang, L. P. Liang, P. Zhang, J. Y. Jin, Y. J. Zhang, T. Y. Ma, and M. Yan, J. Magn. Magn. Mater. **370**, 76 (2014).

[14] T. B. Zhang, X. Q. Zhou, D. D. Yu, Y. Q. Fu, G. J. Li, W. B. Cui, and Q. Wang, Appl. Phys. A: Mater. Sci. Process. **123**, 1 (2017).

[15] Z. W. Liu and J. Y. He, Acta Metall. Sin. (Chin. Ed.). **57**, 1155 (2021).

[16] S. M. Chen, C. F. Liao, B. Q. Cai, X. Wang, Y. F. Jiao, and Y. L. Zeng, Rare Met. Cem. Carbides **48**, 1 (2020).

[17] N. Zou, J. G. Zheng, X. J. Zou, Y. B. Zou, and Y. Q. Zou, Met. Funct. Mater. **23**, 51 (2016).

[18] K. Löewe, C. Brombacher, M. Katter, and O. Gutfleisch, Acta Mater. **84**, 248 (2015).

[19] X. Tang, J. Li, H. Sepehri-Amin, T. Ohkubo, K. Hioki, A. Hattori, and K. Hono, Acta Mater. **203**, 116479 (2021).

[20] C. Liao, X. Zhou, P. Jiang, Z. Zeng, and L. Que, J MAGN. **27**, 172 (2022).

[21] Q. Gong, F. L. Zhang, X. X. Deng, and B. Chen, Chinese Rare Earths. **36**, 120 (2015).

[22] X. L. Liu, Y. J. Zhang, P. Zhang, T. Y. Ma, M. Yan, L. Z. Zhao, and L. W. Li, J. Magn. Magn. Mater. **486**, 165260 (2019).

[23] Y. H. Hou, Y. L. Wang, Y. L. Huang, Y. Wang, S. Li, S. C. Ma, Z. W. Liu, D. C. Zeng, L. Z. Zhao, and Z. C. Zhong, Acta Mater. **115**, 385 (2016).

[24] H. Sepehri-Amin, T. Ohkubo, and K. Hono, J. Appl. Phys. **107**, 09A745 (2010).

[25] M. Soderžnik, K. Ž. Rožman, S. Kobe, and P. McGuiness, Intermetallics, **23**, 158 (2012).

[26] J. Y. Kong, T. H. Kim, S. R. Lee, H. J. Kim, M. W. Lee, and T. S. Jang, Met. Mater. Int. **21**, 600 (2015).

[27] X. H. Cheng, J. Li, L. Zhou, T. Liu, X. J. Yu, and B. Li, J. Chin. Soc. Rare Earths, **37**, 186 (2019).

[28] T. Akiya, J. Liu, H. Sepehri-Amin, T. Ohkubo, K. Hioki, A. Hattori, and K. Hono, J. Appl. Phys. **115**, 17A766 (2014).

[29] H. Sepehri-Amin, L. H. Liu, T. Ohkubo, M. Yano, T. Shoji, A. Kato, T. Schrefl, and K. Hono, Acta Mater. **99**, 297 (2015).